JACS
JOURNAL OF THE AMERICAN CHEMICAL SOCIETY
pubs.acs.org/JACS
Article

Van Der Waals Order−Disorder Type Ferroelectric $VOCl_2$ with Unusual Polarization Switching

Jiapeng Wang,[†] Dong Wang,[†] Zhenjie Guan,[†] Xiangfu Xie, Niuzhuang Yang, Xuzhou Sun, Yuqiang Fang,* Wen He, Zijian Zhang, Jierui Fu, Yue Liu, Ruize Lu, Xingyu Huang, Jinzhong Wang, Peng Tan, Gaoyang Gou, Hao Tian, Yang Ding, Liang Zhen, Fuqiang Huang, Chengyan Xu,* Bo Song,* and Yang Li*

Cite This: https://doi.org/10.1021/jacs.5c16197

Read Online

ACCESS | Metrics & More | Article Recommendations | Supporting Information

ABSTRACT: Harnessing atomic ordering through order−disorder transition is a powerful strategy to tailor electric polarization and functionality. However, most reported order−disorder ferroelectrics exhibit low Curie temperatures, narrow thermal hysteresis, and limited tunability, restricting their potential in nonvolatile memory technologies. Here, we identify $VOCl_2$ as a new van der Waals order−disorder ferroelectric with site disorder, exhibiting an exceptionally wide thermal hysteresis (ΔT = 220 K) and a high Curie temperature (T_c = 440 K), associated with lattice expansion across the disorder to order transition. Moreover, the sensitivity of V^{4+} cations to structure distortions allows efficient polarization tuning under hydrostatic pressure, where pressure irreversibly induces the in-plane polarization at 2.3 GPa, and then drives a reversible polarization switching from in-plane to out-of-plane at 8.0 GPa. Such a giant thermal hysteresis and unusual polarization switching of $VOCl_2$ open new opportunities for programmable phase-change devices with a broad operating window.

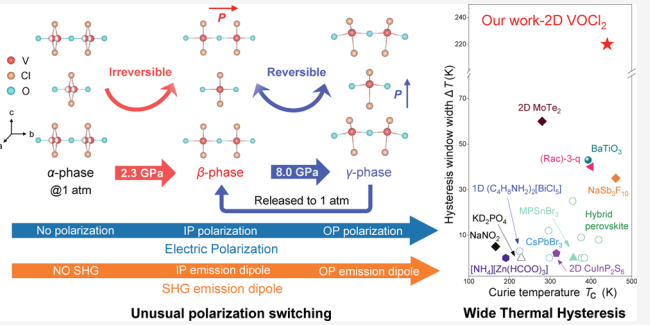

INTRODUCTION

Crystalline materials often exhibit disorder effects such as atomic displacements and orbital occupancy fluctuations. Since such disorder strongly influences the phase structure and symmetry, controlling its degree is crucial for tailoring the functionality of crystalline materials.[1] Over the past decade, regulating and exploiting disorder through disorder−order phase transitions, a variety of fascinating phenomena in ferroelectric, thermoelectric, energy-storage materials have been discovered. For example, modulated piezoelectricity in relaxor ferroelectrics,[2] metal−insulator transition for thermal-switching,[3] the phonon-disorder induced thermal conductivity,[4] offering new strategies for smart sensors, energy conversion, and storage devices. In this context, the frontier of disorder research lies in harnessing the unconventional modes of the disordered state to achieve functionalities unattainable in conventional crystals.[5]

In the study of emerging ferroelectric material, order−disorder transitions represent a crucial mechanism for the ferroelectric−paraelectric transition. Unlike the displacive type ferroelectrics, where robust polarization originates from continuous lattice distortions, order−disorder type ferroelectrics exhibit following unique advantages. First, their lower polarization barrier allows fast response suitable for high-speed memory applications.[6] Second, their soft lattice and intrinsic disorder activate multiple phonon modes, enabling diverse polarization mechanisms such as pseudo Jahn−Teller distortions,[7] lone-pair-electron-driven asymmetric displacements.[8] Third, order−disorder ferroelectrics, such as molecular perovskite[9] and the vdW compound $CuInP_2S_6$[10] possess coordination-bonded or layered lattices that both enhance strain tolerance for flexible electronics and contribute to polarization, thereby providing additional pathways for structural modulation.

Despite these advantages, the reported order−disorder type ferroelectrics still face several critical challenges. For instance, their Curie temperatures are typically low (e.g., T_c = 320 K for $CuInP_2S_6$[11] and T_c = 229 K for KD_2PO_4[12]), primarily due to large vibrational entropy and dominant soft-mode instabilities associated with the disordered lattice, which in turn limiting their high-temperature applications. Moreover, many order−disorder transitions are continuous or second-order-like with

Received: September 15, 2025
Revised: November 18, 2025
Accepted: November 20, 2025

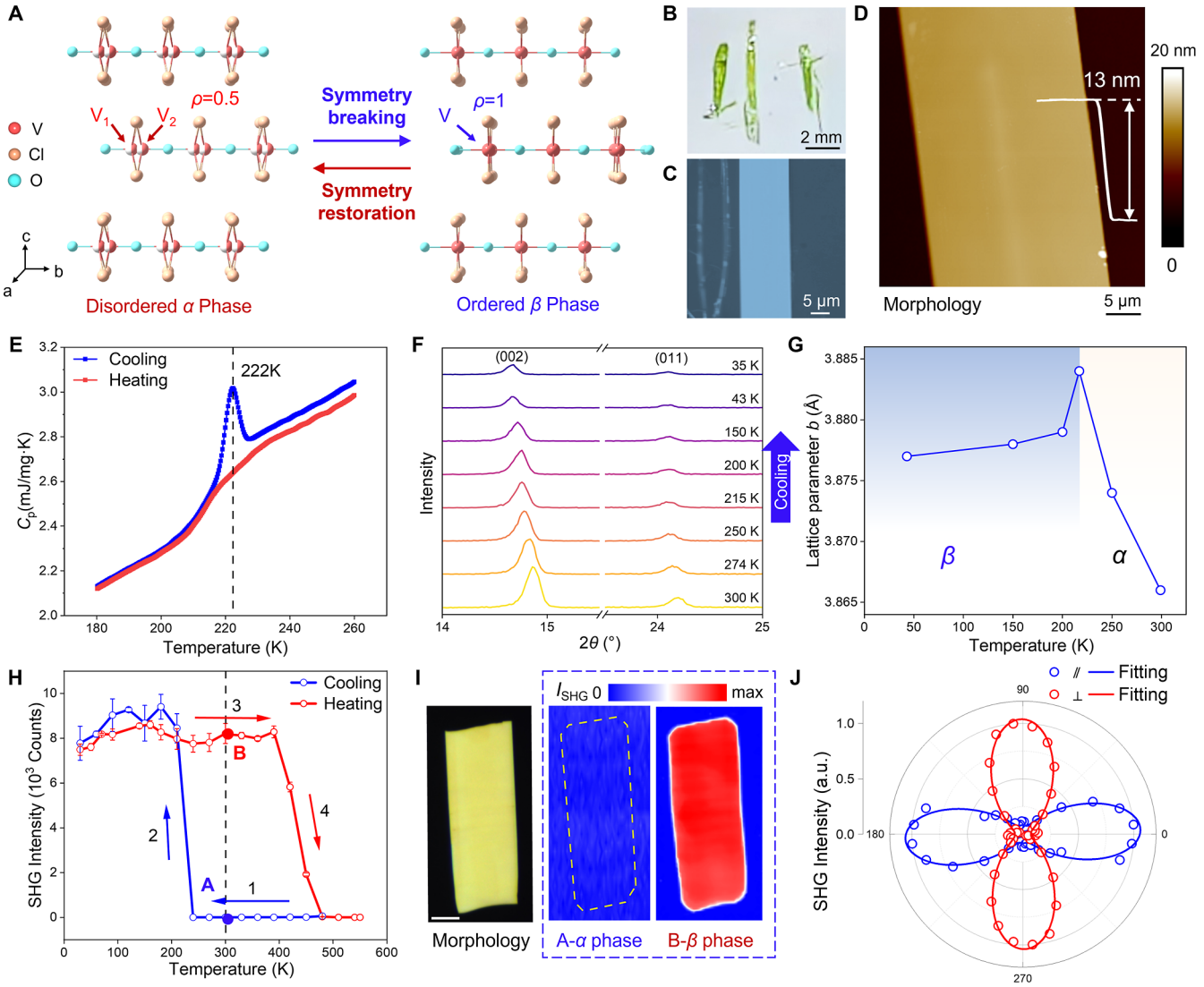

Figure 1. Crystal structure and temperature-induced disorder to order transition in $VOCl_2$. (**A**) Crystal structure of the disordered α-$VOCl_2$ phase and ordered β-$VOCl_2$ phase. (**B**) Photograph of a large green $VOCl_2$ crystal synthesized by chemical vapor transport (CVT). (**C**) Optical image of the exfoliated $VOCl_2$ nanoflakes. (**D**) Representative AFM morphology image of a $VOCl_2$ nanoflake with a thickness of ~13 nm. (**E**) Heat capacity measurements during both cooling and heating cycles. The sharp anomaly at 222 K indicates a first-order phase transition. (F) Temperature-dependent powder X-ray diffraction patterns of $VOCl_2$ with magnified views of the (002) and (011) reflections. (**G**) Evolution of the *b*-axis lattice parameter extracted from temperature-dependent powder XRD measurement, showing a distinct increase corresponding to the α to β phase transition. (**H**) SHG intensity as a function of temperature under thermal cycling, exhibiting a pronounced hysteresis window (ΔT = 220 K) associated with the disorder to order transition. (**I**) Morphology and SHG mapping of the α- and β-phase $VOCl_2$ at the representative temperatures (points A and B, respectively) marked in Figure 1H, illustrating the spatial contrast between the two structural phases. Scale bar: 5 μm. (**J**) Polarization-resolved SHG response of the β-phase measured under parallel and perpendicular configurations.

limited crystallographic rearrangement,[11] exhibiting small thermal hysteresis and a narrow temperature response window, which thereby restricts the stability and controllability of thermally responsive memory and logic devices. To date, research on ferroelectrics with order−disorder behavior has focused mainly on organic−inorganic hybrid perovskites[12−14] and few reported vdW materials ($CuInP_2S_6$).[10] In these systems, polarization switching arises from thermally activated ionic hopping associated with entropy-assisted order−disorder transitions,[15−17] while the tunability of polarization and related physical properties under multiple external stimuli—such as strain, hydrostatic pressure, or light—remains insufficiently explored.

Motivated by these challenges, the vdWs layered transition-metal oxyhalide family MOX_2 (M = V, Nb; X = Cl, Br, I)[18] manifests as a promising candidate for realizing two-dimensional ferroelectricity. In these distorted $[MO_2X_4]$ octahedra, strong orbital coupling induces the pseudo-Jahn−Teller effect, driving the off-center displacement for M^{4+} ions[19] and generating a double-well potential energy surface that underpins ferroelectric behavior.[20] Such local displacements of M^{4+} give rise to diverse functionalities, including tunable nonlinear optical responses[21] and pronounced electro-optic effects.[22] Beyond the local off-centering displacement, however, the ordering of M^{4+} ions are also crucial for tailoring the functional properties, offering new opportunities to overcome the limitations of existing order−disorder ferroelectrics.

In this work, we identify $VOCl_2$ as a new member of the vdW order−disorder ferroelectrics (Figure 1A). Structure analysis reveals that the disordered α-phase exhibits character-

https://doi.org/10.1021/jacs.5c16197
J. Am. Chem. Soc. XXXX, XXX, XXX−XXX

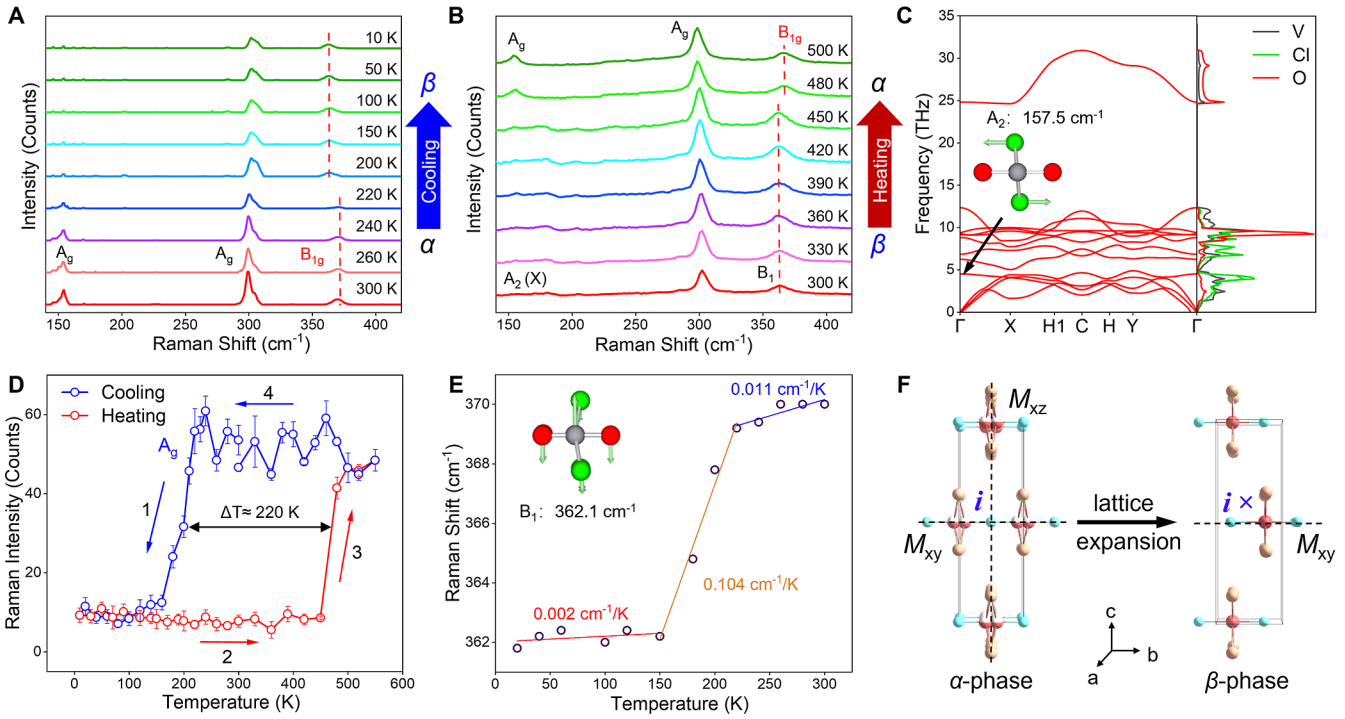

Figure 2. Lattice vibration evolution and thermal hysteresis effect associated with the order−disorder phase transition in $VOCl_2$. (**A**) Raman spectra of the α-phase and in situ temperature-dependent Raman spectra collected during cooling from 300 to 10 K. The disappearance of the A_g mode near 220 K during cooling indicates disordered α-phase to ordered β-phase. (**B**) Temperature-dependent Raman spectra of ordered β-phase (at 300 K) and during heating from 300 to 500 K. The reappearance of the A_g peak near 440 K indicates the reverse $\beta \rightarrow \alpha$ transition. (**C**) Calculated phonon dispersion and phonon density of states (PDOS) for bulk $VOCl_2$. The inset highlights the A_2 phonon mode associated with the structural phase transition. The phonon dispersion is plotted along the high-symmetry path Γ−X−H1−C−H−Y−Γ in the Brillouin zone of the orthorhombic lattice, where H1 and H represent two nonequivalent boundary points along the k_x−k_y plane. (**D**) Temperature-dependent Raman intensities of the A_g mode during both cooling and heating processes, revealing characteristic hysteresis (ΔT = 220 K). (**E**) Raman shifts of B_1 modes as a function of temperature. (**F**) Comparison of symmetry elements between the α- and β-phases and the associated lattice expansion across the transition. In the ordered β-phase, the inversion center i disappears.

istic static site disorder, which undergoes a temperature-driven first-order transition into an ordered β-phase with robust in-plane ferroelectricity. The β-phase features a high Curie temperature (T_c = 440 K) and a giant thermal hysteresis (ΔT = 220 K), both surpassing most reported order−disorder ferroelectrics. Furthermore, the extreme sensitivity of V^{4+} ions to octahedral distortions enables hydrostatic pressure to efficiently tune the crystal symmetry, inducing irreversible in-plane polarization at 2.3 GPa and reversible switching from in-plane to out-of-plane polarization above 8.0 GPa. These findings highlight the rich structural tunability and multi-functionality of $VOCl_2$, making it a promising candidate for nonvolatile memory and programmable phase-change devices.

RESULTS AND DISCUSSION

Structural Characterization and Disorder−Order Transition in $VOCl_2$. Bulk $VOCl_2$ was synthesized via the chemical vapor transport method, which yielded shining centimeter-scale green crystals as shown in Figure 1B. Due to the weak van der Waals interaction, bulk $VOCl_2$ can be easily exfoliated to few-layer flakes, referred to as α-$VOCl_2$nanoflakes (Figure 1C and D). In addition, energy-dispersive spectroscopy (EDS) mapping (Figure S1) confirms the uniform elemental distribution, and X-ray photoelectron spectroscopy (XPS) analysis (Figure S2) verifies the d^1 electronic configuration for V^{4+} cation.

After confirming the chemical composition, we examined the crystal structure using single-crystal X-ray diffraction (SCXRD). The structural refinement results show that α-$VOCl_2$ crystallizes in an orthorhombic structure under ambient conditions (space group *Immm*, a = 3.373 Å, b = 3.834 Å, c = 11.738 Å). The crystal characterizes a vdW layered structural framework, in which $[VO_2Cl_4]$ octahedra share edges along the a-axis and corners along the b-axis, while adjacent layers are weakly coupled through vdW interactions. SCXRD analysis of the α-phase at room temperature reveals pronounced disorder of the V^{4+} ions shown in Figure 1A. The electron density is best described by a split-site occupation model (Tables S1−S3). In this model, the V^{4+} ions occupy the Wyckoff 4 g site with 50% occupancy. Within each $[VO_2Cl_4]$ octahedron, the positional disorder can be illustrated by two symmetry-related positions such as V_1 (0.5000, 0.08480, 0.5000) and V_2 (0.5000, −0.08480, 0.5000). Because the cation distribution is shared between these two equivalent positions, the local mirror symmetry is preserved, and the overall structure remains centrosymmetric. Consequently, dipole formation is effectively prohibited, thereby preventing the emergence of electric polarization and ferroelectricity.

To elucidate the origin of disorder in the α-$VOCl_2$, we examined atomic displacement parameters (ADPs) from **SCXRD** (Table S3). The root-mean-square thermal vibration amplitude of V^{4+} ions along the b-axis, denoted as u_{22}, is 0.0714 Å, reflecting the extent of thermally driven positional fluctuations. In comparison, the separation between the two occupied V^{4+} sites were determined to be d = 0.6500 Å. According to the Nelmes criterion (Text S1),[23,24] since $d/2 \gg$

https://doi.org/10.1021/jacs.5c16197
J. Am. Chem. Soc. XXXX, XXX, XXX−XXX

u_{22}, the V^{4+} ions cannot move dynamically between the two separation sites. Instead, the V^{4+} ions are equally distributed over two symmetry equivalent yet distinct positions, each stabilized in one minimum of a shallow double-well potential created by local electrostatic interaction.[25,26] This provides direct evidence that the α-phase exhibits static site disorder rather than disorder arising from thermal hopping.

Such static disorder provides fertile opportunities for tuning structure and functionality. Given that atomic site occupancy in disordered systems is often highly temperature-dependent,[27,28] we next investigated the temperature-dependent structural evolution of $VOCl_2$ to assess the occurrence of order−disorder transition. As shown in Figure 1E, the total heat capacity (C_p) of the prepared $VOCl_2$ single crystal exhibits a sharp anomaly near − 222 K during the cooling cycle from 300 to 10 K, accompanied by a distinct thermal hysteresis, indicative of a first-order phase transition.[29,30] Furthermore, temperature-dependent powder X-ray diffraction patterns (Figure 1F and Figure S3) show a systematic shift of diffraction peaks toward lower angles upon cooling, corresponding to lattice expansion. Strikingly, the extracted lattice parameter b exhibits a sudden increase near the transition temperature −222 K (Figure 1G). This anomalous behavior is attributed to the ordering of V^{4+} ions, which alleviates local structural frustration and enables bond-length relaxation along the b-axis.

Subsequently, SCXRD measurement was employed to resolve the structure of the newly formed ordered β-phase. The refinement results are shown in Figure 1A and summarized in Table S1. In stark contrast to the disordered α-phase, the β-phase exhibits complete absence of site disorder, confirming the temperature-driven disorder to order transition. In the ordered β-phase, V^{4+} ions undergo a pseudo-Jahn−Teller effect induced distortion along the b-axis, which breaks the original mirror symmetry and establishes a 2-fold rotational (C_2) axis along the b-axis, ultimately giving rise to an in-plane spontaneous polarization (P_s).

Considering the β-phase is noncentrosymmetric while the α-phase is centrosymmetric, second-harmonic generation (SHG) provides an effective probe of their symmetry differences.[31,32] As shown in Figures 1H and S4, the SHG signal of $VOCl_2$ appears below −220 K as inversion symmetry is broken during the $\alpha \rightarrow \beta$ transition, and vanishes above −440 K during the reverse $\beta \rightarrow \alpha$ transition. This wide thermal hysteresis (ΔT = 220 K) enables reversible switching between ordered and disordered states by changing the thermal path, allowing access to two robust phases with distinct functionalities. For example, SHG mappings of $VOCl_2$ at 300 K for the two states are shown in Figure 1I. The α-phase (marked as A in Figure 1H) exhibits no detectable SHG signal, whereas the β-phase (marked as B in Figure 1H) displays a uniform SHG distribution across the entire flake. Moreover, the polarization-resolved SHG pattern of the β-phase (Figure 1J) further reveals pronounced anisotropy, in contrast to the absence of SHG in the α-phase (Figure S5), consistent with the noncentrosymmetric point group C_{2v}.

Phonon Evolution and Thermal Hysteresis during Order−Disorder Transition. In addition to symmetry breaking, the order−disorder transition strongly modifies lattice vibrations. To probe this effect, we performed in situ temperature-dependent Raman spectroscopy to track the phonon evolution in $VOCl_2$. Guided by group-theoretical analysis (Text S2), we first assigned the irreducible representations of all Raman-active modes in the α-phase. Subsequently, the Raman spectra were collected during cooling from 300 to 10 K, as shown in Figure 2A. Across the $\alpha \rightarrow \beta$ transition near 220 K, two prominent anomalies appear: the A_1 mode vanishes abruptly, while the B_{1g} mode undergoes a pronounced redshift. Owing to the large thermal hysteresis effect, these β-phase features persist upon heating back to 300 K (Figure S7). Besides, an opposite behavior of $\beta \rightarrow \alpha$ temperature is observed near 440 K, characterized by the re-emergence of the A_1 mode and a sharp blueshift of the B_{1g} mode in Figure 2B. These results reveal that both vibrational modes are strongly coupled to the order−disorder transition.

To understand why these modes are sensitive to the transition, we analyzed the phonon density of states (PDOS) obtained from first-principles calculations. The absence of imaginary frequencies across the Brillouin zone confirms the dynamic stability of the structure (Figure 2C). Notably, a phonon vibration mode at 157.5 cm^{-1} appears at the Γ point. While its frequency is close to that of the A_g mode in the disordered α-phase, in the ordered β-phase it is reassigned to the A_2 irreducible representation. This mode involves opposite lateral displacements of neighboring Cl atoms, characteristic of a shear-like vibration. The Raman tensor of A_2 mode in the β-phase $VOCl_2$ (space group Im2m) contains only the off-diagonal xz component, rendering it inactive under typical backscattering geometries with both incident and scattered light polarized in the xy plane. This explains the absence of this mode in the Raman spectra of β-phase $VOCl_2$.

In contrast, in the disordered α-phase $VOCl_2$, the same vibration mode belongs to the A_g and contributes to the diagonal components of the Raman tensor, making it Raman-active under the same measurement geometry. Consequently, the 157.5 cm^{-1} (A_g) phonon mode serves as a sensitive spectroscopic probe to distinguish between the disordered α-phase and the ordered β-phase of $VOCl_2$. Its Raman intensity changes abruptly at ∼220 K and ∼440 K during thermal cycling as shown in Figure S7, directly tracking the reversible disorder to order transition. Consistently, temperature-dependent Raman and SHG measurements reveal an exceptionally wide thermal hysteresis of ∼220 K (Figure 2D), far exceeding that reported for inorganic oxides, hybrid organic−inorganic perovskite and other vdW ferroelectrics with order−disorder transitions shown in.

To elucidate the origin of the giant thermal hysteresis, we focused on the B_1 mode, which exhibits pronounced temperature dependence in Raman peak position. First-principles calculations identify this mode as a bending vibration of V and Cl atoms along the interlayer c-axis (Figure 2E, inset), and symmetry reduction across the transition confirms its correspondence to the B_{1g} mode in the disordered α-phase. Experimentally, the B_{1g} mode shows an anomalous redshift upon cooling, and it also softens under applied pressure, which is unusual because compressing the lattice normally hardens phonon frequencies.[33,34] Moreover, the distinct slopes of its frequency−temperature dependence in the α and β phases during cooling further reveal their different lattice anharmonicity and phonon-volume coupling. Specifically, the temperature derivative of the phonon frequency can be expressed as[35]

$$\frac{d\omega_i}{dT} = -\frac{\gamma_i \omega_i}{V}\frac{dV}{dT}$$

https://doi.org/10.1021/jacs.5c16197
J. Am. Chem. Soc. XXXX, XXX, XXX−XXX

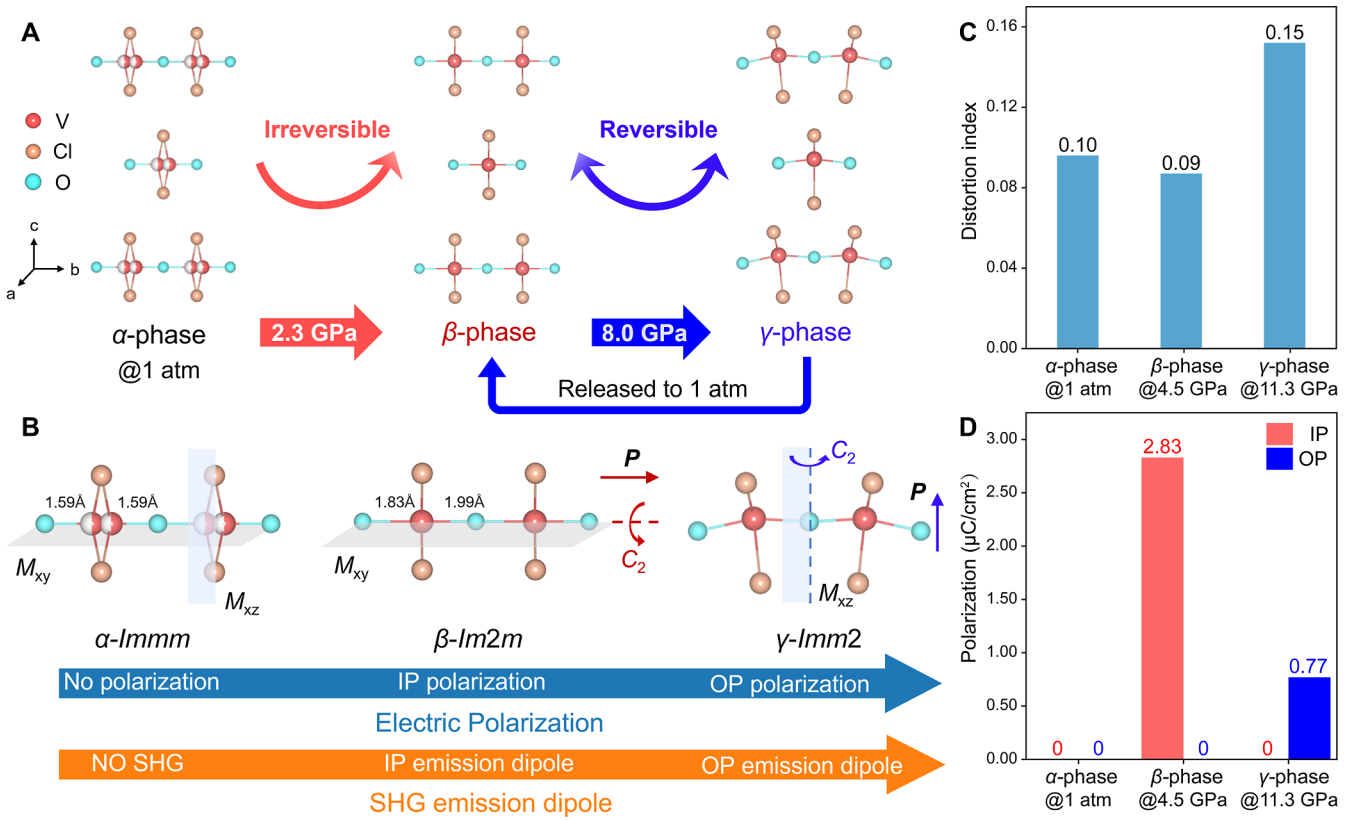

Figure 3. Pressure induced phase transition and structural changes of octahedral unit in vdW $VOCl_2$. (**A**) Crystal structures derived from single-crystal X-ray diffraction, with arrows indicating the transition pathways and corresponding pressures. The $\alpha \rightarrow \beta$ transition at 2.3 GPa is irreversible, whereas the $\beta \rightarrow \gamma$ transition at 8.0 GPa is reversible. Specifically, upon releasing pressure from above 8.0 GPa to ambient conditions (1 atm), the γ-phase irreversibly reverts to the β-phase, which exhibits robust in-plane ferroelectricity. (**B**) Pressure-induced changes in the $[VO_2Cl_4]$ octahedral unit, symmetry elements, and the resulting functionalities. (**C**) Baur's distortion index (D) of the $[VO_2Cl_4]$ octahedral units extracted from SCXRD results for the α, β, γ-$VOCl_2$. (**D**) Calculated electric polarization along the in-plane (IP) and out-of-plane (OP) directions for the α, β, γ-$VOCl_2$.

where ω_i is the phonon frequency, γ_i is the mode Grüneisen parameter, V is the unit-cell volume, and dV/dT represents the thermal evolution of the volume. Experimentally, the slope within the $\alpha \rightarrow \beta$ transition region reaches about 0.104 cm^{-1}/K, much larger than that of the α phase (0.011 cm^{-1}/K) and β phase (0.002 cm^{-1}/K) shown in Figure 2E. This sharp slope enhancement suggests that the phonon anomaly originates from the drastic lattice-volume change associated with the disorder to order transition.

Consistently, single-crystal XRD analysis reveals an expansion of the lattice across the $\alpha \rightarrow \beta$ transition (Figure 2F). According to nonlinear martensitic transformation theory, such a sudden lattice discontinuity leads to strain accumulation and elevated transformation barriers, thereby giving rise to the giant thermal hysteresis.[36] Besides, the intrinsically weak interlayer van der Waals coupling in $VOCl_2$ suppresses strain relaxation, further amplifying the hysteresis window.[37] The combination of a broad temperature tunability in both polarization and phonon responses makes $VOCl_2$ a promising platform for phonon- and polarization-based logic and memory devices.

Pressure-Induced Transitions and Unusual Polarization Switching Behavior. In addition to temperature, hydrostatic pressure is another key thermodynamic variable that can directly modify interatomic distances and bonding states by altering interatomic interactions.[38,39] We first conducted in situ Raman spectroscopy to investigate the pressure-induced phase transition. At 2.3 GPa, the disorder to order transition is triggered, and the β-phase is stabilized with the same ordered structure as that induced by cooling. Subsequently, under the higher pressure about 8.0 GPa, a new stable γ-phase (space group $Imm2$) emerges.

To determine the structure of the new phase, in situ SCXRD measurements were performed at two characteristic pressures, 4.5 and 12.5 GPa (Figure 3A and Table S4). Structural refinement and subsequent analysis reveal that pressure-driven structural evolution not only expands the accessible phase space but also endows the system with enhanced functionalities, such as switchable polarization and tunable SHG emission dipole (Figure 3B). The structural origin of these transitions lies in the distortion of the $[VO_2Cl_4]$ octahedra under compression (Figure 3C). This distortion alters orbital hybridization, thereby modulating both the magnitude and orientation of the local polarization, as illustrated in Figure 3D.

To gain further insight into these pressure-driven transitions, the evolution of phonon modes was tracked by in situ Raman spectroscopy shown in Figure 4A and B. There are three distinct stages upon compression and the corresponding peak shift slopes have been extracted as shown in Figure S8. In the first stage, from ambient pressure to 2.3 GPa, the A_g mode (302.1 cm^{-1}) exhibits a blueshift, while the B_{1g} mode (371.9 cm^{-1}) shows an anomalous redshift, and the A_g mode at 157.5 cm^{-1} vanishes near 2.3 GPa—mirroring the characteristic behaviors of the temperature-induced order−disorder tran-

https://doi.org/10.1021/jacs.5c16197
J. Am. Chem. Soc. XXXX, XXX, XXX−XXX

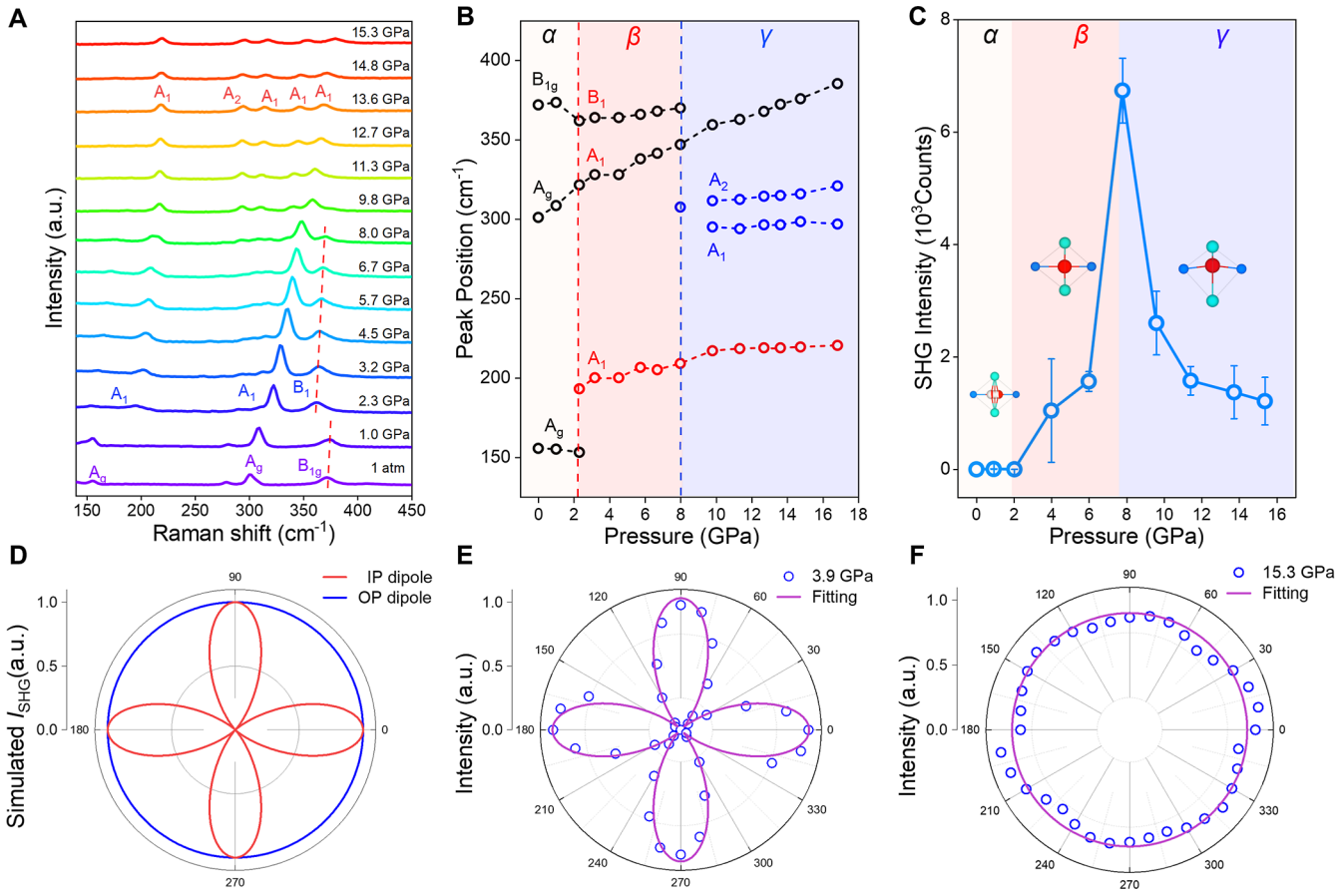

Figure 4. Structural evolution and pressure-induced SHG emission dipole orientation changes of $VOCl_2$ under hydrostatic pressure. (**A**) Raman spectra of $VOCl_2$ nanoflakes at selected pressures, measured at ambient temperature. (**B**) Pressure dependence of Raman frequencies, highlighting significant phase transition behavior at 2.3 and 8.0 GPa. (**C**) Pressure-dependent SHG intensity of $VOCl_2$ nanoflake. (**D**) Simulated polarization-dependent SHG intensity of OP and IP emission dipole for $VOCl_2$ nanoflake. (**E**) Polar plot of the polarization-dependent SHG intensity of $VOCl_2$ nanoflake under 3.9 GPa, showing the occurrence of IP SHG emission dipole. (**F**) Polar plot of the polarization-dependent SHG intensity of $VOCl_2$ nanoflake under 15.3 GPa, showing the occurrence of IP SHG emission dipole.

sition shown in Figure 2A. In the second stage from 2.3 and 8.0 GPa, all phonon modes display blueshifts. Angle-resolved Raman spectra measured at 5.7 and 11.3 GPa (Text S3) reveal distinct polarization-dependent features, indicative of an additional structural transition occurring near 8.0 GPa. In the third stage, from 8.0 to 18.0 GPa, most phonon modes continue to blueshift, while two new peaks appear near 300 cm^{-1} at 8.0 GPa. Overall, the pressure-dependent phonon analysis confirms two critical phase transitions in $VOCl_2$, occurring at 2.3 and 8.0 GPa, respectively.

The structural evolution and the position of V^{4+} during the pressure-driven phase transitions were further examined by revisiting the SCXRD results of $VOCl_2$ at 4.5 and 12.5 GPa. At 4.5 GPa, the split-site behavior of V^{4+} vanishes, marking the completion of the disorder to order transition and the stabilization of the β-phase. This process removes the original 50% site distribution and breaks the mirror symmetry perpendicular to the b-axis, thereby inducing centrosymmetry breaking. Upon further compression to 12.5 GPa, β-$VOCl_2$ undergoes a displacive-type phase transition to γ-$VOCl_2$, with lattice reconstruction and the unit cell multiplicity (Z) increasing from 2 to 8. Simultaneously, the c-axis contracts significantly, from 11.7593 Å at ambient pressure to 10.245 Å at 12.5 GPa. This compression enhances vibronic coupling, amplifying local asymmetry and driving a displacement of V^{4+} ions from the b-axis toward the c-axis.[40] The γ-phase is therefore characterized by stronger structural distortion and a more pronounced off-center displacement of V^{4+} along c-axis.

To quantify the amplitude of structural distortion, we employed Baur's distortion index D[41] to evaluate the deformation within the $[VO_2Cl_4]$ octahedral units of the $VOCl_2$ crystal.

$$D = \frac{1}{n}\sum_{i=1}^{1}\frac{|l_i - l_{av}|}{l_{av}}$$

where l_i represents the bond length between the central atom and the l_i atom, and l_{av} is the average bond length. Typically, pressure-induced distortion could increase bond length anisotropy and lower the structural symmetry, leading to an increase of the distortion index D.[42,43] However, this trend does not apply to the disorder-to-order phase transition in $VOCl_2$. As shown in Figure 3C, for the α-phase under ambient conditions, the V^{4+} ions remain disordered, leading to pronounced variations in V−O and V−Cl bond lengths and resulting in a relatively high distortion index (D) of 0.096. Upon the pressure-induced transition to the β-phase at 4.5 GPa, the V^{4+} ions become ordered and this ordering process partially "freezes" the octahedral distortion, as the previously uneven bond lengths rearrange into a more symmetric configuration, thereby reducing the D value from 0.096 to

https://doi.org/10.1021/jacs.5c16197
J. Am. Chem. Soc. XXXX, XXX, XXX−XXX

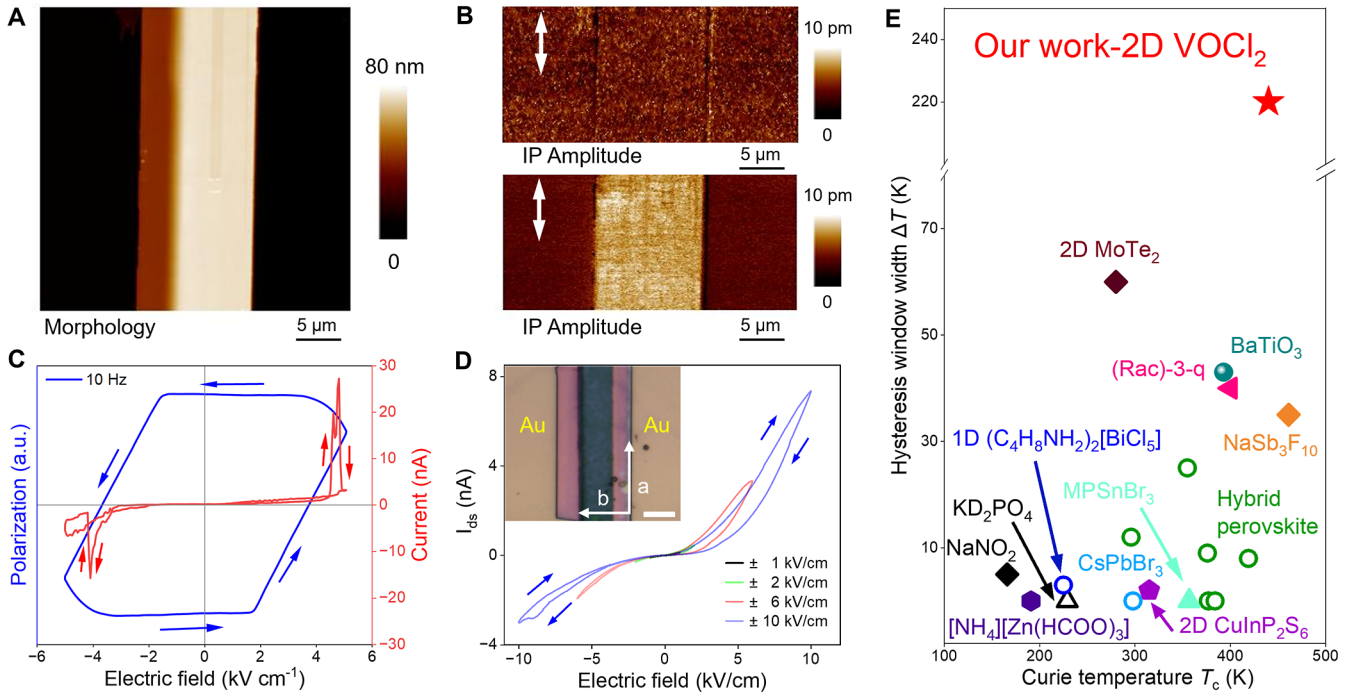

Figure 5. Characterization of room-temperature ferroelectric β-$VOCl_2$ after disorder to order transition. (**A**) Morphology of temperature induced ordered β-$VOCl_2$ nanoflake. (**B**) In-plane piezoresponse force microscopy (PFM) amplitude images of the pristine α-phase (top) and temperature induced ordered β-phase (bottom) The white double arrows indicate the scanning direction of the AFM tip. (**C**) Polarization-electric field (P–E) and current–electric field (I–E) hysteresis loops in lateral β-$VOCl_2$ devices, showing the character of in-plane ferroelectricity. (**D**) β-$VOCl_2$-based ferroelectric 2-terminal device (inset, scale bar = 5 μm) and representative I_{ds}–V_{ds} hysteresis loops measured under different voltage sweep ranges, with sweep directions indicated by arrows. (**E**) Comparison of hysteresis window widths (ΔT) and Curie temperatures for $VOCl_2$ and representative order–disorder-type ferroelectric systems.

0.087. As the pressure reaches to 12.5 GPa, the ordered V^{4+} exhibit a displacement along the c-axis, enhancing the octahedral off-center displacement. This structure transition amplifies the distortion asymmetry, resulting in a higher distortion index D of 0.152 and a more pronounced octahedral distortion under high pressure.

Pressure-Induced Evolution of the SHG Emission Dipole. This pressure-driven octahedral distortion plays a crucial role in modulating local electric dipole polarization and SHG response.[44] To establish the relationship between pressure-induced symmetry changes and optical response, we conducted in situ pressure-dependent SHG measurements shown in Figure 4C. In the centrosymmetric α phase (below 2.3 GPa), no SHG signal is detected. Once the pressure exceeds 2.3 GPa, a disorder to order transition from α-phase to β-phase takes place, breaking inversion symmetry and giving rise to a progressive increase in SHG intensity. The SHG signal reaches its maximum at 8.0 GPa. Upon further compression, the nanoflake undergoes a β-phase to γ-phase transition, and the SHG intensity gradually decreases.

To gain deeper insight into the origin of pressure-dependent SHG intensity, we performed Berry phase calculations shown in Figure 3D to evaluate the evolution of the dipole moment (μ) under pressure along two principal crystallographic directions: the out-of-plane and the in-plane direction. In the centrosymmetric α-phase, no intrinsic dipole moment exists due to its inversion symmetry. Upon transition to the β-phase, the displacement of V^{4+} along the V–O–V direction disrupts the original mirror symmetry perpendicular to the b-axis, replacing it with a 2-fold rotational symmetry (C_2) along the b-axis. This symmetry breaking leads to the emergence of an in-plane ferroelectric polarization magnitude of 2.83 $\mu C/cm^2$. With further compression, pronounced structural deformation drives a pronounced off-center displacement of V^{4+} in the c-axis, shifting the 2-fold rotational symmetry axis from in-plane to out-of-plane orientation. This structural transformation breaks the mirror symmetry perpendicular to the c-axis, leading to the formation of the γ phase, characterized by a dominant out-of-plane polarization. The calculated out-of-plane polarization magnitude in this phase is 0.77 $\mu C/cm^2$, approximately one-fourth of that in the β-phase, correlating with the observed reduction in the SHG intensity.

Beyond the changes in SHG intensity and electric dipole amplitude, the structural symmetry evolution during the phase transition also influences the orientation of the SHG emission dipole, which can be directly characterized by polarization-dependent SHG measurements.[45] Based on the derivation of second-order susceptibility coefficients under different symmetry operations shown in Text S4, β-$VOCl_2$ is predicted to exhibit a pure in-plane (IP) emission dipole, attributed to the second-order susceptibility coefficients χ_{xxy}, χ_{yxx}, χ_{yyy}. In contrast, γ-$VOCl_2$ supports only out-of-plane (OP) dipole component, with only χ_{zxx} and χ_{zyy} contributing to the SHG response. Under backscattering conditions, the polarization-dependent SHG intensity can be expressed as

$$I_{SHG} = I_{IP} + I_{OP} \propto (2\chi_{xxy}\cos\theta\sin\theta + \chi_{yxx}\cos^2\theta + \chi_{yyy}\sin^2\theta)^2 + C$$

where θ represents the rotation angle between the excitation polarization orientation and the x-axis (a-axis) of the crystal lattice, while C is an angle-independent constant, representing

https://doi.org/10.1021/jacs.5c16197
J. Am. Chem. Soc. XXXX, XXX, XXX–XXX

the contribution of the OP emission dipole component to the total SHG signal. Based on eq 3, the simulated angle-resolved SHG in Figure 4D reveals that the SHG intensity of the IP components follows a 4-fold pattern, whereas the SHG intensity of the OP components exhibits an angle-independent circular pattern.[46,47]

As shown in Figure 4E and F, at 3.9 GPa the β-$VOCl_2$ exhibits a 4-fold polarization-resolved SHG pattern dominated by in-plane dipole emission, with only a negligible out-of-plane component (C = 0.02). In contrast, at 15.3 GPa the γ-$VOCl_2$ shows a markedly larger C = 0.80, indicating that the SHG response for γ-$VOCl_2$ is dominated by OP emission dipole. These results demonstrate that the pressure-induced rotation of the symmetry axis governs both the electric polarization and the orientation of the SHG emission dipole.

After establishing the pressure-induced phase transition sequence in $VOCl_2$, a critical question arises: could the pressure-induced phase and its functional properties be retained under ambient conditions? To explore this, the γ-$VOCl_2$ phase stabilized at 15.3 GPa was released back to ambient pressure. The selected area electron diffraction (SAED) pattern of the released γ-$VOCl_2$ closely matches the simulated SAED pattern of the β-phase (Figure S11). Moreover, the Raman spectra and SHG response of the released γ-phase exhibit features consistent with those of the thermally induced β-phase (Figure S12), further confirming the structural and symmetry assignment. To elucidate the origin of the β-phase stability after pressure release, first-principles total-energy calculations were performed. The results reveal that the β-phase is 117 meV per formula unit lower in energy than the γ-phase at ambient pressure (Figure S12C), confirming the intrinsic stability of β-$VOCl_2$ once the applied pressure is released to ambient conditions. Together, these results demonstrate a reversible $\gamma \rightarrow \beta$ transition and an irreversible $\beta \rightarrow \alpha$ transition upon pressure release as summarized in Figure 3A.

Achieving Stable Ferroelectricity via Disorder−Order Transition. To further demonstrate the functional consequence of the disorder−order transition, we examined the ferroelectric response of β-phase $VOCl_2$ using piezoresponse force microscopy (PFM) to probe the IP ferroelectricity. Figure 5A shows the topography of a temperature induced β-$VOCl_2$ nanoflake with 70 nm-thickness, and the corresponding in-plane amplitude images of the α- and β-phases are shown in Figure 5B, respectively. The β-phase exhibits a clear IP piezoelectric response, with phase contrast and amplitude exceeding 5 pm, whereas the α-phase shows no detectable piezoelectric signal (details in Figure S13). Subsequently, angle-resolved PFM measurements shown in Supplementary Text S5 reveal a sinusoidal dependence of the PFM amplitude on the angle between the tip scan direction and the short axis of the nanoflake, indicating the presence of spontaneous in-plane polarization aligned along the short crystallographic for β-$VOCl_2$ nanoflakes.

After confirming the presence of spontaneous polarization, we further verified ferroelectricity by locally switching the polarization using an atomic force microscope (AFM) tip. As shown in Text S6, a DC bias of 8 V was applied by the AFM tip to write a line and a dot on a 14 nm-thick β-$VOCl_2$ nanoflake. After the bias writing, we observed clear line and dot domains exhibiting a 180° phase contrast relative to the pristine regions, while the corresponding topography remained unchanged. The observed switching behavior is further supported by our first-principles calculations of the double-well energy barrier in Figure S17. The bias-controlled domain provides direct evidence of reversible in-plane ferroelectric switching in β-$VOCl_2$.

With the microscopic evidence of ferroelectricity established, we carried out macroscopic polarization−electric field (P−E) hysteresis measurements on fabricated lateral $VOCl_2$ devices (optical image in Figure S18). The $VOCl_2$ nanoflake was carefully aligned and transferred onto the Cr/Au electrodes, with its short axis oriented perpendicular to the channel to ensure the field was applied along the polarization direction. As shown in Figure 5C, the β-phase $VOCl_2$ nanoflake exhibits a P−E hysteresis loop at a driving frequency of 10 Hz. Consistently, the current−electric field (I−E) curve shows a sharp switching-current peak at the coercive field E_c = 4.6 kV cm^{-1}, confirming polarization reversal during the electric-field sweep. Additional P−E loops measured at different frequencies (Figure S18) remain well-defined with discernible remanent polarization and gradually narrow as the frequency increases, consistent with the frequency-dependent domain-switching kinetics in ferroelectrics.[48]

In addition to capacitor-type devices, we further investigated its potential in rectifying components by fabricating a ferroelectric diode based on β-phase $VOCl_2$ (optical image in the inset of Figure 5D). The I_{ds}−V_{ds} curves were measured under lateral electric fields ranging from ±1 kV cm^{-1} to ±10 kV cm^{-1}. At low fields ($|E|$ < 6 kV cm^{-1}), the curves exhibit a clear rectifying behavior, which indicates the presence of a Schottky contact at the electrode-semiconductor interface. When the lateral field exceeds 6 kV cm^{-1}, clockwise hysteresis loops appear under different maximum sweep voltages, indicating that this field surpasses the coercive field, enabling polarization reversal behavior. Besides, the curves show distinct hysteresis windows that gradually expand with increasing sweep voltage, displaying the typical characteristics of a ferroelectric memristor.[10,49] This behavior is attributed to polarization-switching induced modulation of the Schottky barrier height, with the detailed mechanism discussed in Text S7.

We then evaluated the ferroelectricity of $VOCl_2$ induced by pressure. Since the γ-phase reverts to the β-phase once hydrostatic pressure is released to ambient conditions, it is challenging to investigate the ferroelectricity of the γ-phase within a diamond anvil cell (DAC). Therefore, we focused on investigating the ferroelectric behavior of the β-phase. Figure S20 presents the PFM measurement of a β-phase nanoflake exfoliated from the bulk crystal releasing from 15.8 GPa to ambient pressure, where a pronounced PFM amplitude contrast relative to the substrate is clearly observed in the mapping image. Moreover, the butterfly shaped amplitude hysteresis under applied tip bias provides direct evidence of in-plane ferroelectricity.

According to our results, both temperature and hydrostatic pressure serve as effective stimuli for driving the disorder to order transition ($\alpha \rightarrow \beta$) in $VOCl_2$, yielding a room-temperature-stable β-phase with robust in-plane ferroelectricity with a giant thermal hysteresis (ΔT = 220 K) and a high Curie temperature (T_c = 440 K), surpassing those of previously reported inorganic oxides,[50−52] hybrid organic−inorganic perovskites[53−55] and vdW ferroelectrics with order−disorder behavior (Figure 5E).[56−58] The combination of a highly tunable disorder to order transition and controllable octahedral distortions makes $VOCl_2$ a versatile platform for engineering

https://doi.org/10.1021/jacs.5c16197
J. Am. Chem. Soc. XXXX, XXX, XXX−XXX

ferroelectricity and nonlinear optical responses in vdW disordered systems.

CONCLUSIONS

In summary, we identify $VOCl_2$ as a new member of the vdW order−disorder type ferroelectric and demonstrate that its disordered α-phase undergoes a first-order transition to an ordered β-phase under both temperature and pressure stimuli. This transition features an exceptionally large thermal hysteresis (ΔT = 220 K), while the resulting β-phase exhibits robust in-plane ferroelectricity with a Curie temperature exceeding 440 K. Moreover, we show that ferroelectric $VOCl_2$ displays unusual polarization tunability, with hydrostatic pressure acting as an effective nonthermal control: stabilizing the β-phase at 2.3 GPa and further driving a displacive transition to a γ-phase at 8.0 GPa. Across the $\alpha \rightarrow \beta \rightarrow \gamma$ transitions, both the polarization and the SHG emission dipole undergo a unique three-state evolution, from absence to in-plane orientation and ultimately to out-of-plane orientation. These findings establish $VOCl_2$ as a functionally versatile vdW ferroelectric, whose properties can be precisely modulated by external stimuli, offering strong potential for nonvolatile memory and programmable phase-change device applications.

EXPERIMENTAL SECTION

Materials Synthesis. $VOCl_2$ crystals were synthesized using a chemical vapor transport method. The reagents V (Adamas-beta, 99.9%), V_2O_5 (Adamas-beta, 99.9%), and $VOCl_3$ (Adamas-beta, 99.9%) were mixed in a stoichiometric ratio of $VOCl_2$. The mixture was then sealed in an evacuated silica tube, which was heated from 673 to 573 K at a rate of 1 K/min and maintained at that temperature for 5 days. Pale green $VOCl_2$ crystals could be obtained in the growth region. Using Scotch tape, bulk $VOCl_2$ was mechanically exfoliated and then transferred onto target substrates of varying thicknesses.

Characterization of $VOCl_2$ Structure. The microstructure and elemental distributions of the $VOCl_2$ nanoflakes were examined by high-resolution transmission electron microscope (HRTEM) (FEI Tecnai F30). The thickness and surface morphology of $VOCl_2$ were obtained by atomic force microscope (Bruker Dimension Icon PT). The crystal structures of $VOCl_2$ at room temperature were determined by single-crystal X-ray diffraction (XRD). Both ambient- and high-pressure diffraction data were collected on a Bruker D8 VENTURE diffractometer equipped with Mo $K\alpha$ radiation. For the ambient-pressure XRD data, ω- and φ-scan strategies were employed; for the high-pressure XRD data, ω-scan strategy was performed at 2θ = −20°, 0°, and 20°. Absorption corrections were applied using the multiscan method with SADABS.[59,60] The crystal structures were solved with SHELXT and refined with SHELXL, both implemented in the APEX3 software package (Bruker AXS, 2015). The macroscopic ferroelectric hysteresis (P−E loop) was characterized using a TF Analyzer 3000 ferroelectric test system (aixACCT Systems GmbH). The polarization and current data were analyzed using the Vision software package.

Hydrostatic Pressure Experiments. A silicone oil pressure medium was used to ensure quasihydrostatic conditions and minimize fluorescence background. Under an optical microscope, ruby spheres (10−20 μm in diameter) were carefully placed inside the diamond anvil cell (DAC) using a 30 μm tungsten needle for pressure calibration. Pressure-dependent Raman spectra were acquired with a confocal Raman microscope (Renishaw inVia-Reflex) using a 532 nm excitation laser, a 50× Olympus objective, and an 1800 mm^{-1} grating. The laser power incident on the sample was kept below 1 mW to avoid local heating.

SHG Measurement. In situ SHG spectra under varying pressures were recorded in a back-reflection geometry using a homemade femtosecond spectroscopy setup with a 1033 nm excitation laser (pulse width = 80 fs). A 100× Olympus objective was used to focus the beam, and the average incident power was maintained below 0.5 mW. For angle-resolved SHG, both parallel and perpendicular polarization configurations were employed. A polarization analyzer before the detector selected the SHG component parallel or perpendicular to the excitation, while a half-wave plate in the common optical path allowed fine control of the polarization state.

PFM Measurement. In the Piezoelectric force microscopy (PFM) measurement, an AC modulation bias (V_{ac}) was applied to the sample to raise the inverse piezoelectric effect and the tip scanned the sample surface under a normal loading force <10 nN. Besides, the tip used in the experiment is covered with a conductive coating (0.01−0.025 Ω·cm n-doped Si) for electrical conductivity. The cantilevers have spring constants of about 3.1 N/m and free-air resonances at around 75 kHz. Deflection sensitivity was calibrated by recording force−distance curves on a rigid substrate and fitting the linear contact region. The obtained value (133.05 nm/V) was then used to convert the photodetector signal from mV to real displacement. PFM switching spectroscopy was conducted by applying a triangular-wave voltage to the tip while monitoring the PFM amplitude under 3 V AC driving voltage.

First-Principles Calculations. First-principles calculations are performed based on density functional theory (DFT) as implemented in the Vienna ab initio Simulation Package (VASP),[61] using Perdew−Burke−Ernzerhof (PBE) functional within generalized gradient approximation (GGA).[62] A plane-wave basis set within the projector augmented-wave (PAW) method[63] is employed for calculations, using 500 eV plane-wave energy cutoff. Brillouin zone is sampled with 3 × 3 × 3 Monkhorst−pack k-point grids. All crystal structures are fully optimized until the residual Hellmann−Feynman forces are smaller than 0.01 eV/Å and total energy are converged less than 1×10^{-6} eV. The electronic contributions to polarizations of ferroelectric $VOCl_2$ are calculated following the Berry phase method.[64]

ASSOCIATED CONTENT

Supporting Information

The Supporting Information is available free of charge at https://pubs.acs.org/doi/10.1021/jacs.5c16197.

> The Supporting Information provides detailed crystallographic refinements and atomic displacement parameters of α-, β-, and γ-$VOCl_2$ under variable temperature and pressure. It also includes morphology, elemental composition, and XPS characterization of $VOCl_2$ nanoflakes; powder and single-crystal X-ray diffraction analyses; Raman and angle-resolved Raman spectra revealing the order−disorder transition and pressure-induced structural evolution; SHG measurements, mapping, and dipole orientation analyses; TEM and PFM studies of phase transitions; electric-field hysteresis loops and pressure-induced ferroelectricity; schematic diagrams of SHG setups and ferroelectric 2-terminal device devices; comprehensive tabulated crystallographic and spectroscopic data (PDF).

Accession Codes

Deposition Numbers 2488215, 2501713, 2502887, and 2503367 contain the supplementary crystallographic data for this paper. These data can be obtained free of charge via the joint Cambridge Crystallographic Data Centre (CCDC) and Fachinformationszentrum Karlsruhe Access Structures service.

AUTHOR INFORMATION

Corresponding Authors

Yuqiang Fang − *School of Materials Science and Engineering, Shanghai Jiao Tong University, Shanghai 200240, China*; Email: fangyuqiang@sjtu.edu.cn

https://doi.org/10.1021/jacs.5c16197
J. Am. Chem. Soc. XXXX, XXX, XXX−XXX

Chengyan Xu − *Sauvage Laboratory for Smart Materials, School of Materials Science and Engineering, Harbin Institute of Technology (Shenzhen), Shenzhen 518055, China;* orcid.org/0000-0002-7835-6635; Email: cy_xu@hit.edu.cn

Bo Song − *Frontier Science Center for Interaction Between Space Environment and Matter, Harbin 150001, China; Laboratory for Space Environment and Physical Sciences, National Key Laboratory of Laser Spatial Information, Harbin Institute of Technology, Harbin 150001, China;* Email: songbo@hit.edu.cn

Yang Li − *School of Materials Science and Engineering, Harbin Institute of Technology, Harbin 150001, China; Frontier Science Center for Interaction Between Space Environment and Matter, Harbin 150001, China; MOE Key Laboratory of Micro-Systems and Micro-Structures Manufacturing, Harbin Institute of Technology, Harbin 150080, China;* orcid.org/0009-0005-9836-2556; Email: liyang2018@hit.edu.cn

Authors

Jiapeng Wang − *School of Materials Science and Engineering, Harbin Institute of Technology, Harbin 150001, China; Frontier Science Center for Interaction Between Space Environment and Matter, Harbin 150001, China*

Dong Wang − *Center for High-pressure Science &Technology Advanced Research, Beijing 100193, China;* orcid.org/0000-0001-5004-9732

Zhenjie Guan − *School of Materials Science and Engineering, Harbin Institute of Technology, Harbin 150001, China*

Xiangfu Xie − *School of Materials Science and Engineering, Harbin Institute of Technology, Harbin 150001, China*

Niuzhuang Yang − *School of Instrument and Electronics, North University of China, Taiyuan 030051, China*

Xuzhou Sun − *School of Materials Science and Engineering, Shanghai Jiao Tong University, Shanghai 200240, China*

Wen He − *School of Materials Science and Engineering, Harbin Institute of Technology, Harbin 150001, China;* orcid.org/0000-0001-7972-8667

Zijian Zhang − *School of Physics, Harbin Institute of Technology, Harbin 150001, China*

Jierui Fu − *School of Materials Science and Engineering, Harbin Institute of Technology, Harbin 150001, China*

Yue Liu − *School of Materials Science and Engineering, Harbin Institute of Technology, Harbin 150001, China*

Ruize Lu − *School of Materials Science and Engineering, Harbin Institute of Technology, Harbin 150001, China*

Xingyu Huang − *School of Materials Science and Engineering, Harbin Institute of Technology, Harbin 150001, China*

Jinzhong Wang − *School of Materials Science and Engineering, Harbin Institute of Technology, Harbin 150001, China*

Peng Tan − *School of Physics, Harbin Institute of Technology, Harbin 150001, China;* orcid.org/0000-0001-9563-9744

Gaoyang Gou − *Frontier Institute of Science and Technology & State Key Laboratory of Electrical Insulation and Power Equipment, Xi'an Jiaotong University, Xi' An 710049, China;* orcid.org/0000-0003-1485-8115

Hao Tian − *School of Physics, Harbin Institute of Technology, Harbin 150001, China;* orcid.org/0000-0003-1909-7511

Yang Ding − *Center for High-pressure Science &Technology Advanced Research, Beijing 100193, China*

Liang Zhen − *School of Materials Science and Engineering, Harbin Institute of Technology, Harbin 150001, China; Sauvage Laboratory for Smart Materials, School of Materials Science and Engineering, Harbin Institute of Technology (Shenzhen), Shenzhen 518055, China;* orcid.org/0000-0001-6159-8972

Fuqiang Huang − *School of Materials Science and Engineering, Shanghai Jiao Tong University, Shanghai 200240, China;* orcid.org/0000-0003-0526-5473

Complete contact information is available at: https://pubs.acs.org/10.1021/jacs.5c16197

Author Contributions

[††]These authors contributed equally to this work. All authors contributed to the research, discussed the results, and reviewed the manuscript.

Notes

The authors declare no competing financial interest.

■ ACKNOWLEDGMENTS

The authors would like to thank Dr. Zhaoyuan Sun from the Center of Analysis and Measurement at Harbin Institute of Technology for AFM measurements. The authors are grateful to Dr. Fuyang Liu for his help with the X-ray diffraction experiments. This work was supported by the National Natural Science Foundation of China (Grant Nos. 52225201, 52272146, 52301188). W.H. acknowledges the support from the China Postdoctoral Science Foundation (2024M754161), Y.D. is grateful for support from the National Key Research and Development Program of China (Grant No. 2022YFA1402301). Hefei Advanced Computing Center is acknowledged for its computational support.

■ REFERENCES

(1) Hazen, R. M.; Yang, H. Increased compressibility of pseudobrookite-type $MgTi_2O_5$ caused by cation disorder. *Science* **1997**, *277* (5334), 1965−1967.

(2) Liu, H.; Shi, X.; Yao, Y.; Luo, H.; Li, Q.; Huang, H.; Qi, H.; Zhang, Y.; Ren, Y.; Kelly, S. D.; et al. Emergence of high piezoelectricity from competing local polar order-disorder in relaxor ferroelectrics. *Nat. Commun.* **2023**, *14* (1), 1007.

(3) Shao, Z.; Cao, X.; Luo, H.; Jin, P. Recent progress in the phase-transition mechanism and modulation of vanadium dioxide materials. *NPG Asia Mater.* **2018**, *10* (7), 581−605.

(4) Ortner, T. S. Local order in a disordered Zintl phase boosts its thermoelectric performance. *Commun. Chem.* **2021**, *4* (1), 153.

(5) Simonov, A.; Goodwin, A. L. Designing disorder into crystalline materials. *Nat. Rev. Chem.* **2020**, *4* (12), 657−673.

(6) Sun, Z.; Yi, X.; Tao, K.; Ji, C.; Liu, X.; Li, L.; Han, S.; Zheng, A.; Hong, M.; Luo, J. A. Molecular Ferroelectric Showing Room-Temperature Record-Fast Switching of Spontaneous Polarization. *Angew. Chem., Int. Ed.* **2018**, *57* (31), 9833−9837.

(7) Bersuker, I. On the origin of ferroelectricity in perovskite-type crystals. *Phys. Lett.* **1966**, *20* (6), 589−590.

(8) Zhao, W.-P.; Shi, C.; Stroppa, A.; Di Sante, D.; Cimpoesu, F.; Zhang, W. Lone-pair-electron-driven ionic displacements in a ferroelectric metal−organic hybrid. *Inorg. Chem.* **2016**, *55* (20), 10337−10342.

(9) Xu, W. J.; Li, P. F.; Tang, Y. Y.; Zhang, W. X.; Xiong, R. G.; Chen, X. M. A Molecular Perovskite with Switchable Coordination Bonds for High-Temperature Multiaxial Ferroelectrics. *J. Am. Chem. Soc.* **2017**, *139* (18), 6369−6375.

(10) He, W.; Yang, Y.; Li, C.; Wong, W. P.; Cimpoesu, F.; Toader, A. M.; Wu, Z.; Wu, X.; Lin, Z.; Xu, Q.-h.; et al. Near-90 switch in the

polar Axis of dion−jacobson perovskites by halide substitution. *J. Am. Chem. Soc.* **2023**, *145* (25), 14044−14051.
(11) Liu, F.; You, L.; Seyler, K. L.; Li, X.; Yu, P.; Lin, J.; Wang, X.; Zhou, J.; Wang, H.; He, H.; et al. Room-temperature ferroelectricity in $CuInP_2S_6$ ultrathin flakes. *Nat. Commun.* **2016**, *7* (1), 12357.
(12) Yang, B.; Xie, P.; Car, R. Deuteration removes quantum dipolar defects from KDP crystals. *npj Comput. Mater.* **2024**, *10* (1), 241.
(13) Peksa, P.; Zaręba, J. K.; Ptak, M.; Mączka, M. a.; Gągor, A.; Pawlus, S.; Sieradzki, A. Revisiting a perovskite-like copper-formate framework $NH_4[Cu(HCOO)_3]$: order−disorder transition influenced by Jahn-Teller distortion and above room-temperature switching of the nonlinear optical response between two SHG-active states. *J. Phys. Chem. C* **2020**, *124* (34), 18714−18723.
(14) Bokov, A. A.; Bari, M.; Ye, Z.-G. Incipient ferroelectricity in methylammonium lead halide perovskites. *Commun. Mater.* **2025**, *6* (1), 80.
(15) Xu, Z.; Dong, X.; Wang, L.; Wu, H.; Liu, Y.; Luo, J.; Hong, M.; Li, L. Precisely tailoring a FAPbI3-derived ferroelectric for sensitive self-driven broad-spectrum polarized photodetection. *J. Am. Chem. Soc.* **2023**, *145* (3), 1524−1529.
(16) He, R.; Wang, H.; Liu, F.; Liu, S.; Liu, H.; Zhong, Z. Unconventional ferroelectric domain switching dynamics in $CuInP_2S_6$ from first principles. *Phys. Rev. B* **2023**, *108* (2), 024305.
(17) Chandra, P.; Lonzarich, G. G.; Rowley, S. E.; Scott, J. F. Prospects and applications near ferroelectric quantum phase transitions: a key issues review. *Rep. Prog. Phys.* **2017**, *80* (11), 112502.
(18) Slater, J. C. Theory of the transition in KH_2PO_4. *J. Chem. Phys.* **1941**, *9* (1), 16−33.
(19) Choudhury, R. R.; Panicker, L.; Chitra, R.; Sakuntala, T. Structural phase transition in ferroelectric glycine silver nitrate. *Solid State Commun.* **2008**, *145* (7−8), 407−412.
(20) Helmer, P.; Dahlqvist, M.; Rosen, J. Computational screening of MOX_2 transition metal oxydihalides with M= V, Nb, Ta, Mo, Ru, or Os, and X= Cl, Br, or I. *J. Mater. Chem. C* **2025**, *13* (9), 4769−4780.
(21) Zhang, Y.; Lin, L.-F.; Moreo, A.; Alvarez, G.; Dagotto, E. Peierls transition, ferroelectricity, and spin-singlet formation in monolayer VOI_2. *Phys. Rev. B* **2021**, *103* (12), L121114.
(22) Liu, C.; Zhang, X.; Wang, X.; Wang, Z.; Abdelwahab, I.; Verzhbitskiy, I.; Shao, Y.; Eda, G.; Sun, W.; Shen, L.; et al. Ferroelectricity in niobium oxide dihalides $NbOX_2$ (X= Cl, I): A macroscopic-to microscopic-scale study. *ACS Nano* **2023**, *17* (8), 7170−7179.
(23) Abdelwahab, I.; Tilmann, B.; Wu, Y.; Giovanni, D.; Verzhbitskiy, I.; Zhu, M.; Berté, R.; Xuan, F.; Menezes, L. d. S.; Eda, G.; et al. Giant second-harmonic generation in ferroelectric NbOI2. *Nat. Photonics* **2022**, *16* (9), 644−650.
(24) Zhang, Z.; Di, X.; Paillard, C.; Bellaiche, L.; Jiang, Z. Giant electro-optic and elasto-optic effects in ferroelectric $NbOI_2$. *Phys. Rev. B* **2024**, *110* (10), L100101.
(25) Nelmes, R. Structural studies of KDP and the KDP-type transition by neutron and X-ray diffraction: 1970−1985. *Ferroelectrics* **1987**, *71* (1), 87−123.
(26) Ichikawa, M.; Gustafsson, T.; Olovsson, I. Is $NaNO_2$ a pure order−disorder type ferroelectric? *Solid State Commun.* **2002**, *123* (3−4), 135−139.
(27) Støckler, K. A. H.; Roth, N.; Feidenhans'l, A. A.; Takahashi, S.; Nishibori, E.; Iversen, B. B. Models of polaron fluctuations in $LuFe_2O_4$. *Phys. Rev. Mater.* **2024**, *8* (3), 034409.
(28) Nicolson, A.; Breternitz, J.; Kavanagh, S. R.; Tomm, Y.; Morita, K.; Squires, A. G.; Tovar, M.; Walsh, A.; Schorr, S.; Scanlon, D. O. Interplay of Static and Dynamic Disorder in the Mixed-Metal Chalcohalide $Sn_2SbS_2I_3$. *J. Am. Chem. Soc.* **2023**, *145* (23), 12509−12517.
(29) Beutler, A.; Lundgren, E.; Nyholm, R.; Andersen, J.; Setlik, B.; Heskett, D. Coverage-and temperature-dependent site occupancy of carbon monoxide on Rh (111) studied by high-resolution core-level photoemission. *Surf. Sci.* **1998**, *396* (1−3), 117−136.
(30) Dixit, V.; Nandadasa, C. N.; Kim, S.-G.; Kim, S.; Park, J.; Hong, Y.-K.; Liyanage, L. S.; Moitra, A. Site occupancy and magnetic properties of Al-substituted M-type strontium hexaferrite. *J. Appl. Phys.* **2015**, *117* (24), 243904.
(31) Gascoin, F.; Maignan, A. Order−disorder transition in $AgCrSe_2$: a new route to efficient thermoelectrics. *Chem. Mater.* **2011**, *23* (10), 2510−2513.
(32) Malick, S.; Świątek, H.; Bławat, J.; Singleton, J.; Klimczuk, T. Large magnetoresistance and first-order phase transition in antiferromagnetic single-crystalline $EuAg_4Sb_2$. *Phys. Rev. B* **2024**, *110* (16), 165149.
(33) Fichera, B. T.; Kogar, A.; Ye, L.; Gökce, B.; Zong, A.; Checkelsky, J. G.; Gedik, N. Second harmonic generation as a probe of broken mirror symmetry. *Phys. Rev. B* **2020**, *101* (24), 241106.
(34) Wang, Y.; Xiao, J.; Yang, S.; Wang, Y.; Zhang, X. Second harmonic generation spectroscopy on two-dimensional materials. *Opt. Mater. Express* **2019**, *9* (3), 1136−1149.
(35) Mittal, R.; Chaplot, S.; Schober, H.; Mary, T. Origin of negative thermal expansion in cubic ZrW_2O_8 revealed by high pressure inelastic neutron scattering. *Phys. Rev. Lett.* **2001**, *86* (20), 4692.
(36) Ye, M.; Lacmann, T.; Frachet, M.; Vinograd, I.; Garbarino, G.; Maraytta, N.; Merz, M.; Heid, R.; Haghighirad, A.-A.; Le Tacon, M. Anomalous phonon Grüneisen parameters in the semiconductor Ta_2NiS_5. *Phys. Rev. B* **2024**, *110* (3), 035120.
(37) Yang, M.; Cheng, X.; Li, Y.; Ren, Y.; Liu, M.; Qi, Z. Anharmonicity of monolayer MoS_2, $MoSe_2$, and WSe_2: A Raman study under high pressure and elevated temperature. *Appl. Phys. Lett.* **2017**, *110* (9), 093108.
(38) Liang, Y. G.; Lee, S.; Yu, H. S.; Zhang, H. R.; Liang, Y. J.; Zavalij, P. Y.; Chen, X.; James, R. D.; Bendersky, L. A.; Davydov, A. V.; et al. Tuning the hysteresis of a metal-insulator transition via lattice compatibility. *Nat. Commun.* **2020**, *11* (1), 3539.
(39) Lv, B. Q.; Zong, A.; Wu, D.; Rozhkov, A. V.; Fine, B. V.; Chen, S. D.; Hashimoto, M.; Lu, D. H.; Li, M.; Huang, Y. B.; et al. Unconventional Hysteretic Transition in a Charge Density Wave. *Phys. Rev. Lett.* **2022**, *128* (3), 036401.
(40) Tse, J. S. A chemical perspective on high pressure crystal structures and properties. *Natl. Sci. Rev.* **2020**, *7* (1), 149−169.
(41) Ahmed, M. I.; Biswas, A.; Asif, T. I.; Saiduzzaman, M.; Islam, M. Hydrostatic pressure-induced transformations and multifunctional properties of Francium-based halide perovskite $FrCaCl_3$: Insights from first-principles calculations. *Heliyon* **2024**, *10* (13), No. e34059.
(42) Girshberg, Y.; Yacoby, Y. Ferroelectric phase transitions and off-centre displacements in systems with strong electron-phonon interaction. *J. Phys.: Condens. Matter* **1999**, *11* (48), 9807.
(43) Baur, W. The geometry of polyhedral distortions. Predictive relationships for the phosphate group. *Acta Crystallogr., Sect. B: Struct. Crystallogr. Cryst. Chem.* **1974**, *30* (5), 1195−1215.
(44) Kesari, S.; Garg, A. B.; Clemens, O.; Joseph, B.; Rao, R. Pressure-induced structural behavior of orthorhombic $Mn_3(VO_4)_2$: Raman spectroscopic and X-ray diffraction investigations. *ACS Omega* **2022**, *7* (3), 3099−3108.
(45) Zhao, J.; Ross, N.; Angel, R. Tilting and distortion of $CaSnO_3$ perovskite to 7 GPa determined from single-crystal X-ray diffraction. *Phys. Chem. Miner.* **2004**, *31* (5), 299−305.
(46) Lin, K.; Gong, P.; Chu, S.; Li, Q.; Lin, Z.; Wu, H.; Wang, Q.; Wang, J.; Kim, M. J.; Kato, K.; et al. Strong Second Harmonic Generation in a Tungsten Bronze Oxide by Enhancing Local Structural Distortion. *J. Am. Chem. Soc.* **2020**, *142* (16), 7480−7486.
(47) Su, H.; Liu, X.; Wei, C.; Li, J.; Sun, Z.; Liu, Q.; Zhou, X.; Deng, J.; Yi, H.; Hao, Q.; et al. Pressure-Controlled Structural Symmetry Transition in Layered InSe. *Laser Photonics Rev.* **2019**, *13* (6), 1900012.
(48) Petrić, M. M.; Villafañe, V.; Herrmann, P.; Ben Mhenni, A.; Qin, Y.; Sayyad, Y.; Shen, Y.; Tongay, S.; Müller, K.; Soavi, G.; et al. Nonlinear Dispersion Relation and Out-of-Plane Second Harmonic Generation in MoSSe and WSSe Janus Monolayers. *Adv. Opt. Mater.* **2023**, *11* (19), 2300958.

https://doi.org/10.1021/jacs.5c16197
J. Am. Chem. Soc. XXXX, XXX, XXX−XXX

(49) Hu, J.; Hossain, M. E.; Li, J. Investigation on frequency-dependent hysteresis loops of ferroelectric materials. *Smart Mater. Struct.* **2019**, *28* (12), 125002.
(50) Xue, F.; He, X.; Retamal, J. R. D.; Han, A.; Zhang, J.; Liu, Z.; Huang, J. K.; Hu, W.; Tung, V.; He, J. H.; et al. Gate-tunable and multidirection-switchable memristive phenomena in a van der Waals ferroelectric. *Adv. Mater.* **2019**, *31* (29), 1901300.
(51) Xu, X.; Zhong, T.; Zuo, N.; Li, Z.; Li, D.; Pi, L.; Chen, P.; Wu, M.; Zhai, T.; Zhou, X. High-T_C two-dimensional ferroelectric $CuCrS_2$ grown via chemical vapor deposition. *ACS Nano* **2022**, *16* (5), 8141−8149.
(52) Mimura, T.; Shimizu, T.; Kiguchi, T.; Akama, A.; Konno, T. J.; Katsuya, Y.; Sakata, O.; Funakubo, H. Effects of heat treatment and in situ high-temperature X-ray diffraction study on the formation of ferroelectric epitaxial Y-doped HfO_2 film. *Jpn. J. Appl. Phys.* **2019**, *58* (SB), SBBB09.
(53) Yamada, Y.; Shibuya, I.; Hoshino, S. Phase transition in $NaNO_2$. *J. Phys. Soc. Jpn.* **1963**, *18* (11), 1594−1603.
(54) Ravel, B.; Stern, E.; Vedrinskii, R.; Kraizman, V. Local structure and the phase transitions of BaTiO3. *Ferroelectrics* **1998**, *206* (1), 407−430.
(55) Zhang, Y. Q.; Li, M.; Xu, G. C. Phase Transition and Dielectric Response Originating from Disorder-Order Transition in the In-Based Organic-Inorganic Hybrid Material $[NH_3(CH_2)_5NH_3][InCl_5(H_2O)]\cdot H_2O$. *Eur. J. Inorg. Chem.* **2021**, *2021* (13), 1251−1255.
(56) Weyerstahl, P.; Marschall, H.; Schulze, M.; Schwope, I. Synthesis of rac-Presilphiperfolan-9-ol. *Liebigs Annalen* **1996**, *1996* (5), 799−807.
(57) Xu, G. C.; Ma, X. M.; Zhang, L.; Wang, Z. M.; Gao, S. Disorder-order ferroelectric transition in the metal formate framework of $[NH_4][Zn(HCOO)_3]$. *J. Am. Chem. Soc.* **2010**, *132* (28), 9588−9590.
(58) Christie, R.; Wu, P.; Photinos, P.; Abrahams, S. Phase transitions and ferroelectricity in NaSb3F10. *Applied Crystallography* **2009**, *42* (1), 58−62.
(59) Zhou, L.; Xu, K.; Zubair, A.; Zhang, X.; Ouyang, F.; Palacios, T.; Dresselhaus, M. S.; Li, Y.; Kong, J. Role of Molecular sieves in the CVD synthesis of large-area 2D $MoTe_2$. *Adv. Funct. Mater.* **2017**, *27* (3), 1603491.
(60) Gu, Q.-J.; Tong, Y.-Q.; Yin, S.-Q.; Wang, P.; Gong, P.-P.; Li, Y.-J.; Fang, Y.; Zhao, Y.; Huang, B. A one-dimensional organic−inorganic hybrid ferroelectric exhibiting a dielectric-optical duple switch. *J. Mater. Chem. C* **2025**, *13* (8), 3759−3763.
(61) Blessing, R. H. An empirical correction for absorption anisotropy. *Acta Crystallogr. A* **1995**, *51* (1), 33−38.
(62) Krause, L.; Herbst-Irmer, R.; Stalke, D. An empirical correction for the influence of low-energy contamination. *Appl. Crystallogr.* **2015**, *48* (6), 1907−1913.
(63) Kresse, G.; Furthmüller, J. Efficiency of ab-initio total energy calculations for metals and semiconductors using a plane-wave basis set. *Comput. Mater. Sci.* **1996**, *6* (1), 15−50.
(64) Perdew, J. P.; Wang, Y. Accurate and simple analytic representation of the electron-gas correlation energy. *Phys. Rev. B Condens Matter* **1992**, *45* (23), 13244−13249.

https://doi.org/10.1021/jacs.5c16197
J. Am. Chem. Soc. XXXX, XXX, XXX−XXX